

Millimeter- and Submillimeter-Wave Observations of the OMC-2/3 region. IV

Interaction between the Outflow and the Dense Gas in the Cluster Forming Region of OMC-2 FIR 6

YOSHITO SHIMAJIRI^{1,4}, SATOKO TAKAHASHI², SHIGEHISA TAKAKUWA², MASAO
SAITO³, and RYOHEI KAWABE^{4,5} *

¹ *Department of Astronomy, School of Science, University of Tokyo, Bunkyo, Tokyo 113-0033, Japan*

² *Academia Sinica Institute of Astronomy and Astrophysics, P.O. Box 23-141, Taipei 106, Taiwan*

³ *ALMA Project Office, National Astronomical Observatory of Japan, Osawa 2-21-1, Mitaka, Tokyo 181-8588,
Japan*

⁴ *Nobeyama Radio Observatory, Minamimaki, Minamisaku, Nagano 384-1805, Japan*

⁵ *National Astronomical Observatory of Japan, Osawa 2-21-1, Mitaka, Tokyo 181-8588, Japan
yoshito.shimajiri@nao.ac.jp*

(Received <reception date>; accepted <acceptation date>)

Abstract

We have conducted millimeter interferometric observations of the Orion Molecular Cloud-2 (OMC-2) FIR 6 region at an angular resolution of $\sim 4'' - 7''$ with the Nobeyama Millimeter Array (NMA). In the 3.3 mm continuum emission we detected dusty core counterparts of the previously identified FIR sources (FIR 6a, 6b, 6c, and 6d), and moreover, resolved FIR 6a into three dusty cores. The size and mass of these cores are estimated to be 1100-5900 AU and 0.19-5.5 M_{\odot} , respectively. We found that in the ^{12}CO ($J=1-0$) emission FIR 6b, 6c, and 6d eject the molecular outflow and that the FIR 6c outflow also exhibits at least two collimated jet-like components in the SiO ($J=2-1$) emission. At the tip of one of the SiO components there appears abrupt increase of the SiO line width ($\sim 15 \text{ km s}^{-1}$), where the three resolved cores in FIR 6a seem to delineate the tip. These results imply the presence of the interaction and the bowshock front between the FIR 6c molecular outflow and FIR 6a. **If the interaction occurred after the formation of the FIR 6a cores the influence of the FIR 6c outflow on the FIR 6a cores is minimal, since the total gravitational force in the FIR 6a cores ($1.0 - 7.7 \times 10^{-4} M_{\odot} \text{ km s}^{-1} \text{ yr}^{-1}$) is much larger than the outflow momentum flux ($2.4 \times 10^{-5} M_{\odot} \text{ km s}^{-1} \text{ yr}^{-1}$). On the other hand, it is also possible that the interaction caused the gravitational instability in FIR 6a, and triggered the fragmentation into three cores, since the separation among these cores ($\sim 2.0 \times 10^3 \text{ AU}$) is on the same order of the Jeans length ($\sim 5.0 - 8.4 \times 10^3 \text{ AU}$). In**

either case, FIR 6a cores, with a mass of 0.18 - 1.6 M_{\odot} and a density of $0.2 - 5.8 \times 10^7 \text{ cm}^{-3}$, might be potential formation sites of the next generation of cluster members.

Key words: stars: formation — stars: individual (OMC-2/FIR 6) — ISM: jets and outflows — ISM: molecules — ISM: cloud

1. INTRODUCTION

Most stars ($\geq 90\%$) form in the mode of cluster formation (Lada & Lada 2003). However, as compared to the isolated star formation (Saito et al. 1999; Saito et al. 2001; Takakuwa et al. 2004; Takakuwa et al. 2007; Jørgensen et al. 2007), the mechanism and the physical process of the cluster formation are still less clear. Previous observational and theoretical studies suggest that some external effects, such as supernovae (Kobayashi et al. 2008) and HII regions (Koenig et al. 2008), are required to trigger cluster formation. **Another candidate of such trigger is a molecular outflow, as proposed both observationally (Sandell & Knee 2001; Yokogawa et al. 2003) and theoretically (Nakamura & Li 2007). The slight increase of the external pressure added by the outflow makes the dense gas gravitationally unstable although it is still close to the equilibrium state, and proceeds the further gravitational fragmentation of the dense gas (Elmegreen 1998), which initiates the formation of stellar clusters (Whitworth et al. 1994).** The observational evidence of triggered star formation, however, have yet been mainly based on morphologies and the detailed discussions of the physical processes are still less comprehensive.

The Orion Molecular Cloud-2/3 (OMC-2/3) region is one of the nearest cluster-forming regions, including intermediate-mass protostars, that has been observed in the infrared, submillimeter, and millimeter bands. (Genzel & Stutzki 1989; Castets & Langer 1995; Chini et al. 1997; Johnstone & Bally 1999; Yu et al. 2000; Lada & Lada 2003; Tsujimoto et al. 2003; Williams et al. 2003; Allen et al. 2007). We have initiated survey observations of this region at millimeter and submillimeter wavelengths with Nobeyama Millimeter Array (NMA) and Atacama Submillimeter Telescope Experiment (ASTE) (see overview by Takahashi et al. 2008a). In this survey, Takahashi et al. (2008b) identified totally fourteen molecular outflows in the ^{12}CO ($J=3-2$) emission, including seven new detections. Comparison between the $850 \mu\text{m}$ dust continuum emission (Johnstone & Bally 1999) and our ^{12}CO ($J=3-2$) outflow results provides two interesting candidates of the interaction between the dusty dense gas and the outflow, namely, FIR-3/4 and FIR 6, both of which are cluster-forming regions. On the other hand, in the MMS 7 region where there is a single intermediate-mass protostar no observational evidence for the outflow-dense gas interaction is found, and the star-formation in MMS 7 is more likely to be in the isolated mode (Takahashi et al. 2006).

These findings have stimulated us to conduct detailed studies of the interaction between molecular outflows and dense gas as one of the possible mechanisms of cluster formation. Our recent ob-

* Last update: May. 18, 2009

servations of the FIR 3/4 region (Shimajiri et al. 2008) revealed that the molecular outflow driven by FIR 3 interacts with the dense gas associated with FIR 4. Furthermore, the 3.3 mm dust-continuum observations with the NMA at a high spatial resolution ($\sim 3''$) have revealed that FIR 4 consists of eleven dusty cores. From the comparison between the core separation and the Jeans length, the fragmentation and the interacting time scale, and between the virial and LTE masses of the dusty cores, we propose that the interaction triggered the fragmentation into these dusty cores, and the next generation of cluster formation in FIR 4.

In order to investigate whether the scenario of the outflow-triggered cluster formation is ubiquitous or a specific case only applicable to FIR 4, it is necessary to search for more samples. In this paper, we report detailed millimeter interferometric observations of the other target, the FIR 6 region in OMC-2 (Chini et al. 1997). In the FIR 6 region, there are five MIR sources and one 3.6 cm VLA source (Reipurth et al. 1999; Nielbock et al. 2003). In this region, we found two molecular outflows driven by FIR 6b and 6c (Takahashi et al. 2008a; Takahashi et al. 2008b), and the outflow driven by FIR 6c appears to interact with the dense molecular gas at FIR 6a seen in the 850 μ m dust continuum emission (Johnstone & Bally 1999). Since this situation of the FIR 6 region is similar to that of the FIR 4 region, the FIR 6 region is a potential site for the outflow-triggered cluster formation.

2. OBSERVATIONS AND DATA REDUCTION

We carried out millimeter interferometric observations of the FIR 6 region in the ^{12}CO ($J=1-0$; 115.271 GHz), SiO ($v=0$, $J=2-1$; 86.847 GHz) lines and in the 3.3 mm continuum emission with the Nobeyama Millimeter Array (NMA), which consists of six 10 m antennas, during a period from 2006 January to 2008 February. The phase reference centers of the ^{12}CO ($J=1-0$) observations are $(\alpha_{J2000}, \delta_{J2000}) = (5^h 35^m 23^s.28, -5^\circ 12' 3''.19)$ and $(5^h 35^m 23^s.46, -5^\circ 13' 15''.20)$, while those of the SiO ($v=0, J=2-1$) and 3.3 mm continuum observations are $(\alpha_{J2000}, \delta_{J2000}) = (5^h 35^m 23^s.38, -5^\circ 12' 19''.19)$ and $(5^h 35^m 20^s.66, -5^\circ 13' 15''.00)$. The molecular line data were obtained with the FX correlator, which was configured with 1024 channels per baseline and a bandwidth of 32 MHz. For the ^{12}CO ($J=1-0$) and SiO ($v=0, J=2-1$) data we made 5 and 10-channel binning to increase the signal-to-noise ratio ($\equiv S/N$) of the high-velocity line-wing emission, providing the velocity resolution in the ^{12}CO and SiO observations of 0.406 km s^{-1} and 1.08 km s^{-1} , respectively. We obtained the continuum data at both the lower ($87.090 \pm 0.512 \text{ GHz}$) and upper ($98.418 \pm 0.512 \text{ GHz}$) sidebands with the digital spectral correlator, Ultra Wide Band Correlator (UWBC, Okumura et al. 2000). To obtain a higher S/N in the continuum map, the data of both sidebands were co-added (effective observing frequency = 92 GHz, corresponding to the wavelength of 3.3 mm).

Using the AIPS package developed at NRAO, we adopted the natural weighting for the imaging of the molecular emissions. For the continuum imaging we adopted both the uniform and natural UV weighting. Table 1 and Table 2 summarize the parameters for the line and continuum observations, respectively. Our observations of the ^{12}CO ($J=1-0$) and SiO ($v=0, J=2-1$) lines were insensitive to structures more extended than $42''.9$ (0.09 pc) and $50''.0$ (0.1 pc) at the 10 % level (Wilner

& Welch 1994), since the minimum projected baseline length of the ^{12}CO ($J=1-0$) and SiO ($v=0$, $J=2-1$) observations was 3.9 and 3.3 k λ , respectively. The overall uncertainty in the flux calibration was estimated to be $\sim 15\%$. After the calibration, only the data taken under good weather conditions were adopted in the imaging.

3. RESULTS

3.1. 3.3 mm Dust Continuum Emission

Figure 1a and 1b show naturally- and uniformly-weighted 3.3 mm dust continuum images in the FIR 6 region, respectively. To make these images, we first CLEANed the South-West and the North-East field individually, and then we corrected them for the primary beam response and combined them with the Miriad task “linmos”. The rms noise levels before the primary beam correction are similar at both field, and we adopted these noise levels as references of the contour levels. From these images, we identified six 3.3 mm continuum condensations with the following criteria; (1) the peak intensity of condensations should be higher than the 3σ noise level, (2) the “valley” among different condensations should be deeper than 1σ , and (3) the structure is consistent between the naturally- and uniformly-weighted images, and the size should be larger than the relevant beam size. Hereafter we call these condensations CORE 1-6, as labeled in Figure 1.

CORE 1, 5, and 6 are associated with FIR 6b, c, and d, which are previously identified in the 1300 μm observations (Chini et al. 1997). CORE 1 (FIR 6b) is also associated with a 24 μm source detected with Spitzer MIPS (ID 36; Takahashi et al. 2008b). CORE 5 is not associated with any MIR source, but shows a cavity-like structure pointing toward FIR 6a in the naturally-weighted 3.3 mm continuum image, whose direction is consistent with the direction of the outflow driven by FIR 6c (see Figure 2a and c). CORE 6 is also associated with a 24 μm source detected with Spitzer MIPS (ID 38; Takahashi et al. 2008b), as well as 5, 10, and 20 μm sources (MIR 30 and 31; Nielbock et al. 2003). This core has an elongated structure toward the SE-NW direction, which coincides with the direction of the molecular outflow driven by FIR 6d traced by the ^{12}CO (1–0) emission (see Figure 2d). Toward FIR 6a, an elongated dusty structure is seen in the naturally-weighted 3.3 mm continuum image. In the uniformly-weighted image, we have resolved FIR 6a into three cores, CORE 2, 3, and 4. These cores do not harbor any MIR sources. Hereafter we call this aggregation FIR 6a clump.

The deconvolved size of each dusty core was estimated by the 2-dimensional Gaussian fitting to the uniformly-weighted image, providing the typical deconvolved size of $\sim 1100 - 5900$ AU. **The total gas + dust mass of the cores ($\equiv M_{\text{dust}}$) was derived from the total 3.3 mm continuum flux (F_ν) in the uniformly-weighted image, on the assumption that all the 3.3-mm continuum emission arises from dusts, the emission is optically thin, and that the gas-to-dust mass ratio is 100, using the formula;**

$$M_{\text{dust}} = \frac{F_\nu d^2}{\kappa_\nu B_\nu(T_d)}, \quad (1)$$

where we adopt a value of the mass opacity, $\kappa_\nu = 0.1 \left(\frac{250\mu m}{\lambda_{92GHz}} \right)^\beta \text{ cm}^2 \text{ g}^{-1}$ (Hildebrand 1983), and **distance $d = 400 \text{ pc}$ (Menten et al. 2007; Sandstrom et al. 2007).** For the dust temperature we adopt the temperature range of $T_d = 20 - 52.7 \text{ K}$. The lower boundary, $T_d = 20 \text{ K}$, is adopted from the typical dust temperature of the OMC-3 cores (Chini et al. 1997) and the higher boundary, $T_d = 52.7 \text{ K}$, is derived from the peak intensity of the $^{12}\text{CO} (J=3-2)$ spectrum toward FIR 6 (see Figure 3).

We adopt $\beta = 2$ for the warm dusty cores in the FIR 6 region, since FIR 6 is located in the same molecular filament of OMC-2 as FIR 1 and FIR 2, where the β value is estimated to be 2 by the spectral energy distribution fitting (Chini et al. 1997). The masses of CORE 1, 2, 3, 4, 5, and 6 are estimated to be 1.9 - 5.5, 0.56 - 1.6, 0.18 - 0.51, 0.52 - 1.5, 1.6 - 4.5, and 1.4 - 4.0 M_\odot , respectively. The mean gas density ($\equiv n$) in these dusty cores was derived by assuming a spherically-symmetric shape as follows;

$$n = \frac{M_{dust}}{\frac{4}{3}\pi \left(\sqrt{\frac{D_{maj}}{2} \times \frac{D_{min}}{2}} \right)^3}, \quad (2)$$

where D_{maj} , and D_{min} are the deconvolved size along the major and minor axes. The typical gas density is $\sim 10^7 \text{ cm}^{-3}$. Table 3 summarizes these physical properties of the identified cores.

3.2. $^{12}\text{CO} (1-0)$ Emission

Figure 2a shows distributions of the high velocity blueshifted ($-9.5 \sim 4.6 \text{ km s}^{-1}$) and redshifted ($16.4 \sim 29.4 \text{ km s}^{-1}$) $^{12}\text{CO} (J=3-2)$ emission in the FIR 6 region. The $^{12}\text{CO} (J=3-2)$ data were taken by Takahashi et al. (2008b). The total velocity range of the $^{12}\text{CO} (J=3-2)$ emission is much wider than that of the $\text{H}^{13}\text{CO}^+ (J=1-0)$ emission ($9.8 \sim 11.9 \text{ km s}^{-1}$; Ikeda et al. 2007), suggesting that the high velocity $^{12}\text{CO} (J=3-2)$ emission traces the molecular outflows. Molecular outflows ejected from FIR 6b and 6c were identified by Takahashi et al. (2008b), although these molecular outflows were not detected in the previous single-dish $^{12}\text{CO} (J=1-0)$ observations (Aso et al. 2000). These molecular outflows were also detected in the NMA $^{12}\text{CO} (J=1-0)$ observations as shown in Figure 2b and 2c, respectively. The NMA observations show a clearer bipolar morphology of the FIR 6b outflow. In particular, a narrow jet-like feature is seen in the blueshifted South-Western lobe. The intensity of the NMA $^{12}\text{CO} (J=1-0)$ outflow driven by FIR 6c, on the other hand, is fainter than that of the ASTE $^{12}\text{CO} (J=3-2)$ outflow, suggesting that the outflow driven by FIR 6c has extended components ($\geq 42''.9 \sim 0.09 \text{ pc}$).

Moreover, we have found a new outflow candidate in the NMA $^{12}\text{CO} (1-0)$ observations, whose driving source is FIR 6d as shown in Figure 2(d). Since the velocity range of this outflow component detected with the NMA is within that of the ambient cloud component observed with the single-dish ASTE telescope (8.9 km s^{-1} to 13.2 km s^{-1}), this outflow component is hidden in the ambient cloud component and undetectable with ASTE. The distribution of the blueshifted and redshifted $^{12}\text{CO} (J=1-0)$ emission around FIR 6d has a clear bipolar morphology, and the velocity range of the $^{12}\text{CO} (J=1-0)$ emission ($7.7 \sim 12.6 \text{ km s}^{-1}$) is larger than that of the H^{13}CO^+ emission

($9.8 \sim 11.9 \text{ km s}^{-1}$, Ikeda et al. 2007). Hence, these bipolar components in the ^{12}CO ($J=1-0$) emission associated with FIR 6d probably trace the molecular outflow.

Figure 3 shows the ^{12}CO ($J=3-2$) line profile averaged within the region delineated by the dashed rectangle in Figure 2a. The high-velocity line wings, arising from the ensemble of these outflows, are evident in this profile. From the peak temperature of this ^{12}CO ($J=3-2$) spectrum, we determined that the upper limit of the gas kinetic temperature in the FIR 6 region is 52.7 K.

3.3. SiO Emission

Figure 4a-d, and e show integrated intensity maps of the SiO ($v=0$, $J=2-1$) emission at four different velocity ranges of $-11.7 \sim -6.3 \text{ km s}^{-1}$, $-5.2 \sim 0.2 \text{ km s}^{-1}$, $1.3 \sim 3.4 \text{ km s}^{-1}$, $4.6 \sim 15.3 \text{ km s}^{-1}$, and the total velocity range, respectively. The method of the multifield imaging is same as that for Figure 1. In the total integrated intensity map of Figure 4e, a well collimated, linearly extended structure with a position angle of 20° is seen in the SiO emission. The South-Western tip of this SiO feature coincides with the position of FIR 6c. In the low velocity range shown in Figure 4d two SiO components can be identified; one is the compact SiO component located close to FIR 6c (Component 1), and the other extending along the North-East to South-West direction located close to FIR 6a and FIR 6b (Component 2). In the higher blueshifted velocity range, Component 1 appears to shift its peak position away from FIR 6c progressively, and the highest velocity peak locates close to FIR 6a (see Figure 4a). On the other hand, there is no such velocity gradient seen in Component 2.

We will discuss the origin of these SiO components in section 4.1.

4. DISCUSSION

4.1. Interaction between the Molecular Outflow Driven by FIR 6c and FIR 6a Clump

In Figure 5, we compare the spatial distribution of the high-velocity ^{12}CO ($J=3-2$) emission, SiO ($v=0$, $J=2-1$) emission, and the 3.3 mm dust continuum emission. The linearly extended feature in the SiO emission coincides well with the blueshifted lobe of the molecular outflow driven by FIR 6c. Since the SiO emission often traces shocked molecular gas caused by the interaction between the primary jet and the ambient molecular gas (Avery & Chiao 1996; Bachiller et al. 1991; Hirano et al. 2006), this SiO emission probably traces the well collimated outflow driven by FIR 6c. Furthermore, CORE 2, 3, and 4 in FIR 6a clump surround the tip of Component 1 in the SiO emission, while the tip of Component 2 locates even more downstream beyond FIR 6a clump. In Figure 6, we show Position - Velocity diagrams of the ^{12}CO ($J=3-2$) and SiO ($v=0$, $J=2-1$) lines along the axis of the FIR 6c outflow. It is obvious that there are two distinct outflow components in the ^{12}CO and SiO emission; the velocity component with the higher blueshifted velocity corresponds to Component 1, while the other lower velocity component located away from FIR 6c corresponds to Component 2. The SiO emission of Component 1 shows significant increase of the line width at the position of FIR 6a clump. This increase of the SiO line width, as well as the shell-like structure in FIR 6a clump at the interface with Component 1, implies the presence of the interaction between the molecular outflow

driven by FIR 6c and FIR 6a clump (Takakuwa et al. 2003; Shimajiri et al. 2008). We suggest that the two distinct SiO components were ejected toward slightly different 3-dimensional directions, as seen in other protostellar jets (Velusamy & Langer 1998; Bachiller et al. 2001), and that the direction of Component 1 matches the direction to FIR 6a clump from FIR 6c. Therefore, the jet component 1 interacts with FIR 6a clump while Component 2 keeps moving freely. On the assumption of the same jet propagation velocity, the lower line of sight velocity of Component 2 implies that the jet axis of Component 2 is **closer** to the plane of the sky than that of Component 1, which is consistent with the larger distance of Component 2 from FIR 6c.

Such an interaction associated with the outflow alters the physical condition of the surrounding medium through the C-type shock (Bergin et al. 1998; Gusdorf et al. 2008). Gusdorf et al. (2008) have reported that a postshock density is 10 - 40 times more than a preshock density from their MHD simulation of the interaction. Since the present gas density of FIR 6a clump is estimated to be $\sim 1.0 - 2.9 \times 10^7 \text{ cm}^{-3}$, the preshock density of FIR 6a clump is $\sim 2.6 - 7.3 \times 10^5 \text{ cm}^{-3}$ on the assumption that a postshock density is 40 times more than a preshock density.

The redshifted counterpart of the SiO emission, on the other hand, was not detected. One of the possible reasons for the non-detection of the SiO emission is that there is not sufficient dense-gas material at the south-west of FIR 6c, and hence the reservoir of the SiO production or amount of dust grains (Bachiller et al. 2001) are not ample enough. In fact, the 1.3 mm dust continuum map in the FIR 6 region by Chini et al. (1997) exhibits that there is asymmetric distribution of dusts around FIR 6c, and that at the south-west of FIR 6c the dust continuum emission becomes fainter while toward the north-east of FIR 6c the dust continuum emission becomes stronger and shows a emission ridge.

4.2. *Effect of the Interaction on the FIR 6a Cores*

In section 4.1., we demonstrate that the outflow driven by FIR 6c interacts with FIR 6a clump. Three cores in FIR 6a clump locate around the tip of the FIR 6c outflow, and it is possible that the interaction affects the physical evolution of these cores. In the following section, we discuss the possible effects of the interaction on these cores.

First, we compare the time scale of the interaction to the time scale of fragmentation of FIR 6a clump to produce the three cores. On the assumption that the interaction time scale $\tau_{interaction}$ is similar to the dynamical time-scale of the FIR 6c outflow, i.e. $\tau_{interaction} \sim \tau_d$, $\tau_{interaction}$ is estimated to be $1.2\text{-}1.9 \times 10^4 \text{ yr}$ (Takahashi et al. 2008b). The time scale of the fragmentation into the cores can be estimated on the assumption that the fragmentation time scale is the sound crossing time; $\tau_{fragmentation} = \frac{\Delta l}{C_{eff}} \sim 1.5 \times 10^4 \text{ yr}$. These two times scales are indistinguishable from each other and hence it is not straightforward to tell whether the interaction takes place before or after the production of the three cores. Then we will discuss the following two cases;

- CASE 1: The FIR 6a cores were formed before the interaction occurs.

- CASE 2: The FIR 6a cores were formed after the interaction occurs.

In CASE 1, the FIR 6a cores could have been formed via spontaneous fragmentation or turbulent fragmentation before the interaction (Inutsuka & Miyama 1997; Li & Nakamura 2004). In this case, the outflow driven by FIR 6c may externally affect the subsequent evolution of these cores. Maury et al. (2009) have compared the total force required to balance the gravity of the dense cores with the outflow momentum flux in the NGC 2264-C region, in order to assess whether the outflows influence the evolution of the neighboring cores. We follow the same argument for our case of the FIR 6 region to investigate whether the blueshifted component of the FIR 6c outflow influences the physical evolution of the FIR 6a cores. The total force needed to balance gravity F_{grav} is expressed as $F_{grav}(R) = G \times M(R)^2 / 2R^2$ (eq.10; Maury et al. 2009). Since the average radius of the FIR 6a cores and the mass are estimated to be $R = 0.0075$ pc and $M(R) = 1.3 - 3.6 M_{\odot}$, respectively (see section 3.1.), F_{grav} is calculated to be $1.0 - 7.7 \times 10^{-4} M_{\odot} \text{ km s}^{-1} \text{ yr}^{-1}$. On the other hand, the outflow momentum flux of the blueshifted component of the FIR 6c outflow F_{flow} is $2.4 \times 10^{-5} M_{\odot} \text{ km s}^{-1} \text{ yr}^{-1}$ (Takahashi et al. 2008b), and hence the total force is ~ 10 times larger than the outflow momentum flux ($F_{grav} \gg F_{flow}$). Therefore, it is unlikely that the interaction with the FIR 6c outflow influences the subsequent physical evolution of the FIR 6a cores. Maury et al. (2009) have also reported that the total momentum flux of eleven outflows in NGC 2264-C is insufficient to prevent the cores from collapsing.

In CASE 2, the FIR 6a cores are considered to have been produced by the interaction. In fact, Whitworth et al. (1994) have demonstrated that the external shock compression could trigger the gravitational fragmentation of dense-gas clumps into cores. Then, we compare the separation among CORE 2, 3, and 4 with the Jeans length in order to investigate whether the fragmentation into the cores is caused by the gravitational instability. The mean projected separation ($\equiv \Delta l$) among the FIR 6a cores, corresponding to the lower limit of the real separation, is $\sim 5''$ ($\sim 2.0 \times 10^3$ AU). The Jeans length ($\equiv \lambda_J$) can be calculated with $\lambda_J = \sqrt{\frac{\pi C_{eff}^2}{Gn}}$ (Nakamura & Li 2007), where C_{eff} , G , and n are the effective sound speed, gravitational constant, and the average gas density of FIR 6a clump, respectively. We adopt a preshock density of $\sim 2.6 - 7.3 \times 10^5 \text{ cm}^{-3}$ as an average gas density n of FIR 6a clump before the interaction. It is difficult, on the other hand, to observationally estimate C_{eff} , since there is no molecular emission, such as H^{13}CO^+ ($J=1-0$) and N_2H^+ ($J=1-0$), associated with FIR 6a clump (Ikeda et al. 2007; Tatematsu et al. 2008). Hence, we simply assume that C_{eff} in FIR 6a clump is same as that in FIR 4 clump ($\sim 0.62 \text{ km s}^{-1}$). With these values, the Jeans length λ_J is estimated to be $5.0 - 8.4 \times 10^3$ AU, which is comparable to the means separation among FIR 6a cores. Then, it is possible that the interaction triggers the Jeans instability in FIR 6a clump, which results in the fragmentation into FIR 6a cores. Furthermore, this interpretation is supported by the distribution of the dusty cores, which appears to delineate the outflow structure.

Our observational results cannot distinguish precisely between CASE 1 and CASE 2. In

either case, however, FIR 6a clump contains three cores with a mass of $0.18 - 1.6 M_{\odot}$ and a density of $0.2 - 5.8 \times 10^7 \text{ cm}^{-3}$, and these cores may be potential formation sites of the next-generation of cluster members.

5. SUMMARY

We have carried out high angular-resolution ($\sim 4''\text{-}7''$) millimeter interferometric observations of the OMC-2 FIR 6 region with the NMA in the ^{12}CO ($J=1\text{--}0$) and SiO ($v=0$, $J=2\text{--}1$) lines as well as the 3.3 mm continuum emission. The main results of our new millimeter observations are summarized as follows;

1. We detected dusty counterparts of FIR 6a-d in the 3.3 mm continuum emission. In particular we have first resolved FIR 6a into three dusty cores and we totally detected six dusty cores. Typical size, mass, and the average gas density of these cores is estimated to be $\sim 1100\text{-}5900 \text{ AU}$, $\sim 0.18 - 5.5 M_{\odot}$, and $\sim 10^7 \text{ cm}^{-3}$, respectively.
2. Our NMA observations in the ^{12}CO ($J=1\text{--}0$) emission have confirmed the presence of molecular outflows driven by FIR 6b and 6c, which were previously identified with Single-dish observations. Furthermore, we have found a new outflow candidate whose driving source is FIR 6d. Previous single-dish observations could not find this outflow, because this outflow is hidden in the ambient cloud component.
3. We detected at least two well-collimated SiO ($v=0$, $J=2\text{--}1$) components aligned along the axis of the blue lobe of the FIR 6c outflow, which probably traces the well-collimated jet components ejected by FIR 6c. One of the SiO components, Component 1, shows a higher blueshifted velocity ($-11.7 \sim 11.0 \text{ km s}^{-1}$) than the other, Component 2 ($3.4 \sim 14.2 \text{ km s}^{-1}$), while the tip of Component 2 locates more distant from the driving source. At the tip of Component 1, the line width of the SiO emission shows abrupt increase and the cores in FIR 6a clump form a shell-like feature, suggesting the presence of the bowshock front. We consider that Component 1 is interacting with FIR 6a clump while Component 2 is propagating to the different direction freely. Figure 7 shows a schematic picture in the FIR 6 region.
4. The estimated time scale of the fragmentation of FIR 6a clump into the three cores ($\sim 1.5 \times 10^4 \text{ yr}$) is similar to the time scale of the interaction between the molecular outflow driven by FIR 6c and FIR 6a clump ($1.2 - 1.9 \times 10^4 \text{ yr}$), and hence we cannot tell whether the fragmentation of FIR 6a clump into the cores occurs before or after the interaction. In the former case, the interaction with the FIR 6c outflow is unlikely to affect the subsequent evolution of the FIR 6a cores, since the momentum flux of the FIR 6c outflow is one order of magnitude smaller than the gravitational force in the FIR 6a cores. In the latter case, it is possible that the interaction between the FIR 6c outflow and FIR 6a clump triggered the fragmentation into the cores by the gravitational instability. In either case, the FIR 6a cores might be potential sites of the next-generation cluster formation in the FIR 6 region.

We are grateful to the staff at the Nobeyama Radio Observatory (NRO) for both operating the NMA and helping us with the data reduction. Nobeyama Radio Observatory is a branch of the National Astronomical Observatory, National Institutes of Natural Sciences, Japan. We thank D. Johnstone for providing us the submillimeter continuum data taken with JCMT. Moreover we acknowledge M. Yamada, N. Ikeda, Y. Kurono, and T. Tsukagoshi for their helpful comments. We also acknowledge the anonymous referee for providing helpful suggestions to improve the paper. Y. Shimajiri was financially supported by Global COE Program "the Physical Sciences Frontier", MEXT, Japan. S. Takahashi is supported by a postdoctoral fellowship of the Institute of Astronomy and Astrophysics, Academia Sinica. This work was supported by Grant-in-Aid for Scientific Research A 18204017. S. Takakuwa acknowledges a grant from the National Science Council of Taiwan (NSC 97-2112-M-001-003-MY2) in support of this work.

References

- Allen, L., et al. 2007, *Protostars and Planets V*, 361
- Aso, Y., Tatematsu, K., Sekimoto, Y., Nakano, T., Umemoto, T., Koyama, K., & Yamamoto, S. 2000, *ApJS*, 131, 465
- Avery, L. W., & Chiao, M. 1996, *ApJ*, 463, 642
- Bachiller, R., Martin-Pintado, J., & Fuente, A. 1991, *A&A*, 243, L21
- Bachiller, R., Pérez Gutiérrez, M., Kumar, M. S. N., & Tafalla, M. 2001, *A&A*, 372, 899
- Bergin, E. A., Neufeld, D. A., & Melnick, G. J. 1998, *ApJ*, 499, 777
- Castets, A., & Langer, W. D. 1995, *A&A*, 294, 835
- Chini, R., Reipurth, B., Ward-Thompson, D., Bally, J., Nyman, L.-A., Sievers, A., & Billawala, Y. 1997, *ApJL*, 474, L135
- Elmegreen, B. G. 1998, *Origins*, 148, 150
- Genzel, R., & Stutzki, J. 1989, *ARA&A*, 27, 41
- Gueth, F., Bachiller, R., & Tafalla, M. 2003, *A&A*, 401, L5
- Gusdorf, A., Cabrit, S., Flower, D. R., & Pineau Des Forêts, G. 2008, *A&A*, 482, 809
- Hildebrand, R. H. 1983, *QJRAS*, 24, 267
- Hirano, N., Liu, S.-Y., Shang, H., Ho, P. T. P., Huang, H.-C., Kuan, Y.-J., McCaughrean, M. J., & Zhang, Q. 2006, *ApJL*, 636, L141
- Ikeda, N., Sunada, K., & Kitamura, Y. 2007, *ApJ*, 665, 1194
- Inutsuka, S.-I., & Miyama, S. M. 1997, *ApJ*, 480, 681
- Johnstone, D., & Bally, J. 1999, *ApJL*, 510, L49
- Jørgensen, J. K., et al. 2007, *ApJ*, 659, 479
- Kobayashi, N., Yasui, C., Tokunaga, A. T., & Saito, M. 2008, *ApJ*, 683, 178
- Koenig, X. P., Allen, L. E., Gutermuth, R. A., Hora, J. L., Brunt, C. M., & Muzerolle, J. 2008, *ApJ*, 688, 1142
- Lada, C. J., & Lada, E. A. 2003, *ARA&A*, 41, 57
- Li, Z.-Y., & Nakamura, F. 2004, *ApJL*, 609, L83
- Maury, A. J., André, P., & Li, Z. -. 2009, arXiv:0902.1379

Menten, K. M., Reid, M. J., Forbrich, J., & Brunthaler, A. 2007, *A&A*, 474, 515
 Nakamura, F., & Li, Z.-Y. 2007, *ApJ*, 662, 395
 Nielbock, M., Chini, R., Müller, S. A. H. 2003, *A&A*, 408, 245
 Okumura, S. K., et al. 2000, *PASJ*, 52, 393
 Reipurth, B., Rodríguez, L. F., & Chini, R. 1999, *AJ*, 118, 983
 Saito, M., Sunada, K., Kawabe, R., Kitamura, Y., & Hirano, N. 1999, *ApJ*, 518, 334
 Saito, M., Kawabe, R., Kitamura, Y., & Sunada, K. 2001, *ApJ*, 547, 840
 Sandstrom, K. M., Peek, J. E. G., Bower, G. C., Bolatto, A. D., & Plambeck, R. L. 2007, *ApJ*, 667, 1161
 Sandell, G., & Knee, L. B. G. 2001, *ApJL*, 546, L49
 Shimajiri, Y., Takahashi, S., Takakuwa, S., Saito, M., & Kawabe, R. 2008, *ApJ*, 683, 255
 Takahashi, S., Saito, M., Takakuwa, S., & Kawabe, R. 2006, *ApJ*, 651, 933
 Takahashi, S., Saito, M., Takakuwa, S., & Kawabe, R. 2008a, *Ap&SS*, 313, 165
 Takahashi, S., Saito, M., Ohashi, N., Kusakabe, N., Takakuwa, S., Shimajiri, Y., Tamura, M., & Kawabe, R. 2008b, *ApJ*, 688, 344
 Takakuwa, S., Kamazaki, T., Saito, M., & Hirano, N. 2003, *ApJ*, 584, 818
 Takakuwa, S., et al. 2004, *ApJL*, 616, L15
 Takakuwa, S., et al. 2007b, *ApJ*, 662, 431
 Tatematsu, K., Kandori, R., Umemoto, T., & Sekimoto, Y. 2008, *PASJ*, 60, 407
 Tsujimoto, M., Koyama, K., Tsuboi, Y., Goto, M., & Kobayashi, N. 2003, *ApJ*, 585, 602
 Velusamy, T., & Langer, W. D. 1998, *Nature*, 392, 685
 Whitworth, A. P., Bhattal, A. S., Chapman, S. J., Disney, M. J., & Turner, J. A. 1994, *A&A*, 290, 421
 Williams, J. P., Plambeck, R. L., & Heyer, M. H. 2003, *ApJ*, 591, 1025
 Wilner, D. J., & Welch, W. J. 1994, *ApJ*, 427, 898
 Yokogawa, S., Kitamura, Y., Momose, M., & Kawabe, R. 2003, *ApJ*, 595, 266
 Yu, K. C., Billawala, Y., Smith, M. D., Bally, J., & Butner, H. M. 2000, *AJ*, 120, 1974

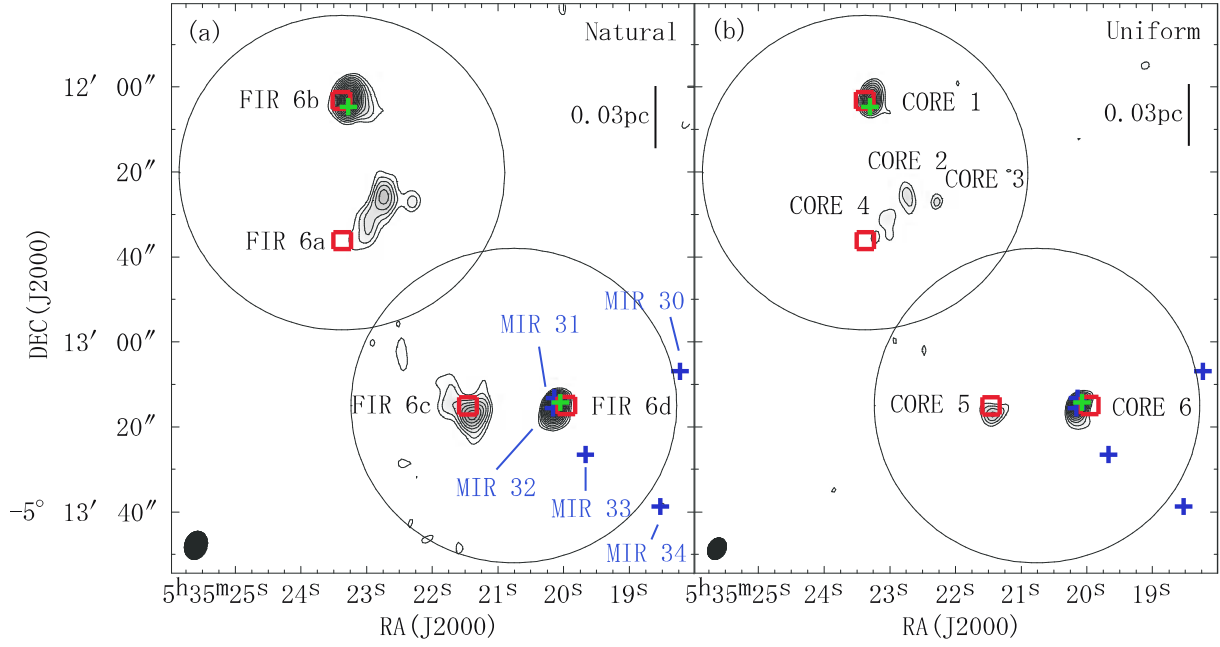


Fig. 1. 3.3 mm dust continuum maps in the FIR 6 region observed with the NMA. The left panel and right shows the naturally-weighted map and uniformly-weighted map. Red squares show the position of the 1.3 mm dust continuum sources, FIR 6a, b, c, and d (Chini et al. 1997). Blue crosses show the position of MIR 30,31,32,33, and 34 (Nielbock et al. 2003). Green crosses show the position of $24 \mu\text{m}$ sources (ID 36 and 38; Takahashi et al. 2008b). Ellipses at the bottom-left corner of each panel show the beam size. Open circles denote the field of view of the NMA observations. Contour levels of panel (a) and (b) start at $\pm 3 \sigma$ noise levels with an interval of 1σ . The rms noise level (1σ) in panel (a) and (b) are 1.0 and $1.2 \text{ mJy beam}^{-1}$, respectively.

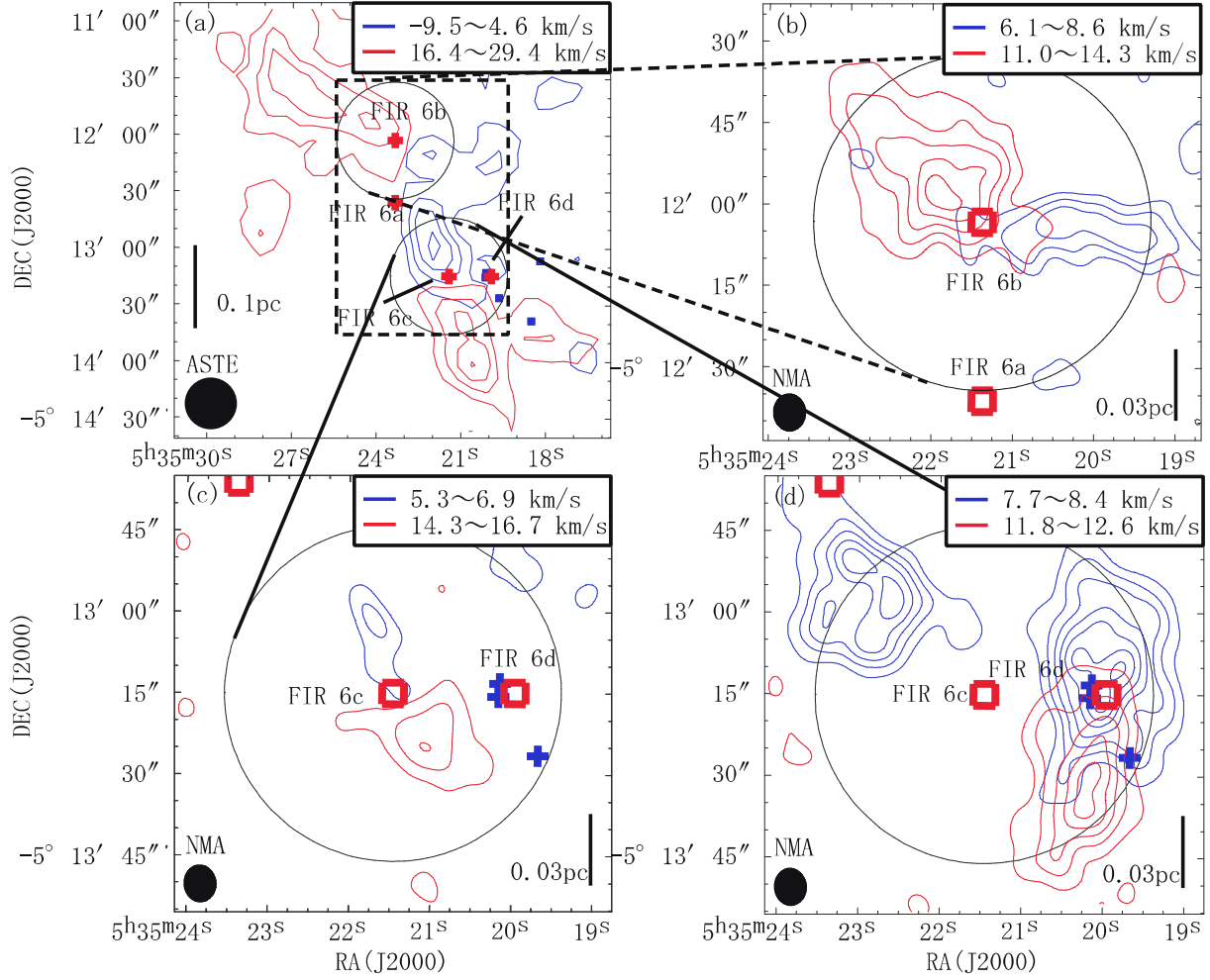


Fig. 2. Distribution of the high-velocity blueshifted (blue contour) and redshifted (red contour) ^{12}CO ($J=3-2$) (the upper left panel) and ^{12}CO ($J=1-0$) emission (the other panels) in the FIR 6 region. Panel (a) shows the distribution of the blue (-9.5 km s^{-1} - 4.6 km s^{-1}) and red (16.4 km s^{-1} - 29.4 km s^{-1}) lobes in the ^{12}CO (3-2) line observed with ASTE (Takahashi et al. 2008b), while panel (b), (c), and (d) show the distribution of blue ($6.1\text{--}8.6$, $5.3\text{--}6.9$, and $7.7\text{--}8.4 \text{ km s}^{-1}$) and red ($11.0\text{--}14.3$, $14.3\text{--}16.7$, and $11.8\text{--}12.6 \text{ km s}^{-1}$) lobes in the ^{12}CO (1-0) line observed with the NMA, respectively. Symbols in the figure are same as in Figure 1. Contour levels of panel (a) start at $\pm 5 \sigma$ levels with an interval of 5σ , while contour levels of panel (b), (c), and (d) start at $\pm 3 \sigma$ levels with an interval of 3σ . The rms noise levels (1σ) in the panel (a), (b), (c), and (d) are $1.2 \times 10^3 \text{ K}$, 0.11, 0.14, and 0.19 Jy beam^{-1} , respectively.

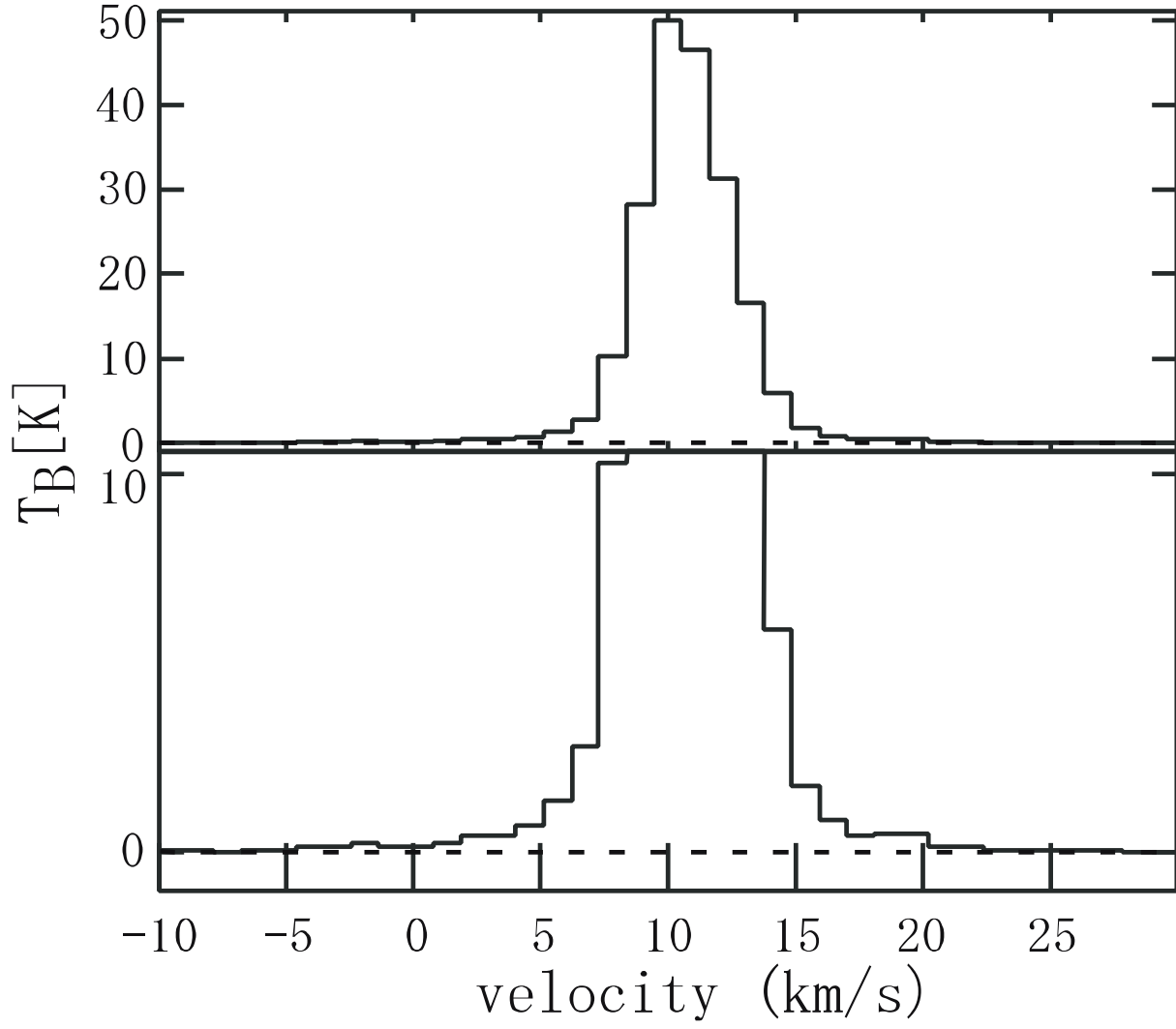


Fig. 3. ^{12}CO ($J=3-2$; 345.705 GHz) spectrum in the FIR 6 region averaged over an area of $2.8' \times 1.5'$ (see Figure 2) taken with ASTE (Takahashi et al. 2008b). The top panel shows the entire spectrum and the bottom panel shows the enlarged view of the line-wing. The rms noise level (1σ) is 0.5 K in T_B at a velocity resolution of 1.1 km s^{-1} .

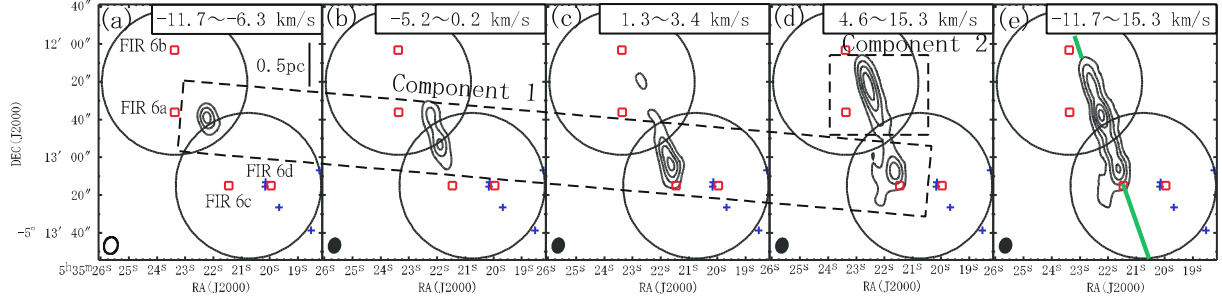


Fig. 4. Spatial and velocity distribution of the SiO ($v=0$, $J=2-1$) emission in the FIR 6 region observed with the NMA. Panel a, b, c, d, and e show the integrated intensity maps of the SiO emission for five different velocity ranges of $-11.7 \sim -6.3 \text{ km s}^{-1}$, $-5.2 \sim 0.2 \text{ km s}^{-1}$, $1.3 \sim 3.4 \text{ km s}^{-1}$, $4.6 \sim 15.3 \text{ km s}^{-1}$, $-11.7 \sim 15.3 \text{ km s}^{-1}$, and total, respectively. Symbols in the figure are same in Figure 1. The green line shows the cut line of the Position-Velocity diagram. Contour levels start at $\pm 10 \sigma$ with an interval of 10σ . The rms noise level (1σ) is 0.126, 0.131, 0.052, 0.151, and 0.225 $\text{Jy beam}^{-1} \text{ km s}^{-1}$ for panel a-e, respectively.

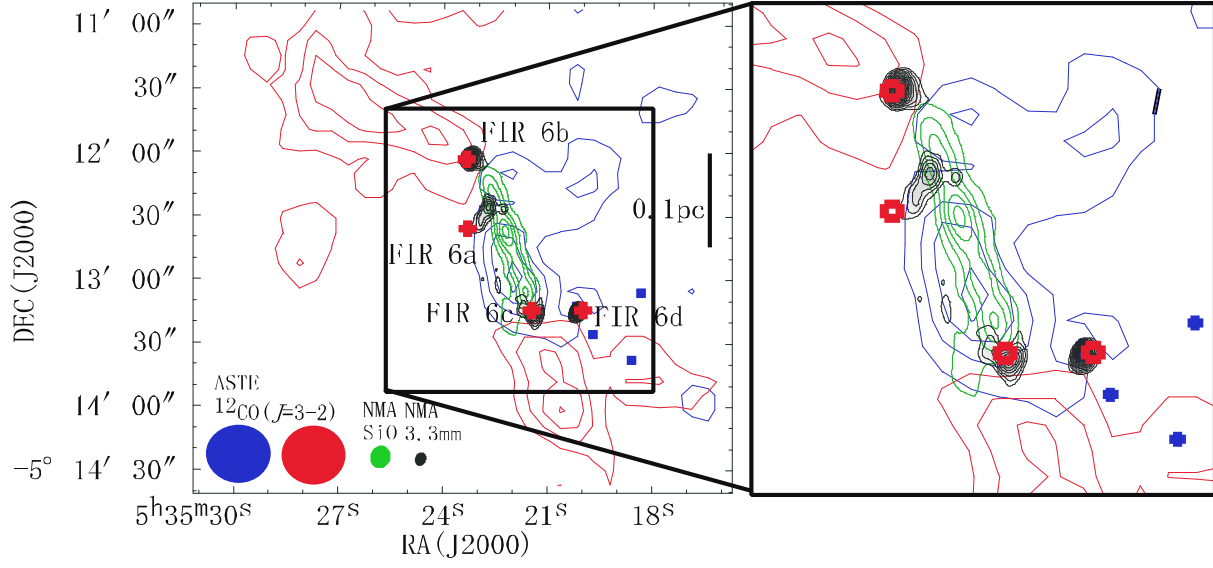


Fig. 5. Comparison of the spatial distribution of the ^{12}CO ($J=3-2$), SiO ($v=0$, $J=2-1$), and the 3.3 mm dust continuum emissions in the FIR 6 region. Red and blue contours show the distribution of the redshifted ($16.4 \sim 29.4 \text{ km s}^{-1}$) and blueshifted ($-9.5 \sim 4.6 \text{ km s}^{-1}$) lobe in the ^{12}CO ($J=3-2$) emission. Green contours show the distribution of the total integrated intensity map of the SiO emission. Black contours show the distribution of the 3.3 mm dust continuum emission. Contour levels of the ^{12}CO ($J=3-2$) emission, SiO ($v=0$, $J=2-1$) emission and the 3.3 mm continuum emission are the same as in Figure 2a, 4e, and Figure 1a, respectively. Symbols in the figure are same as in Figure 1.

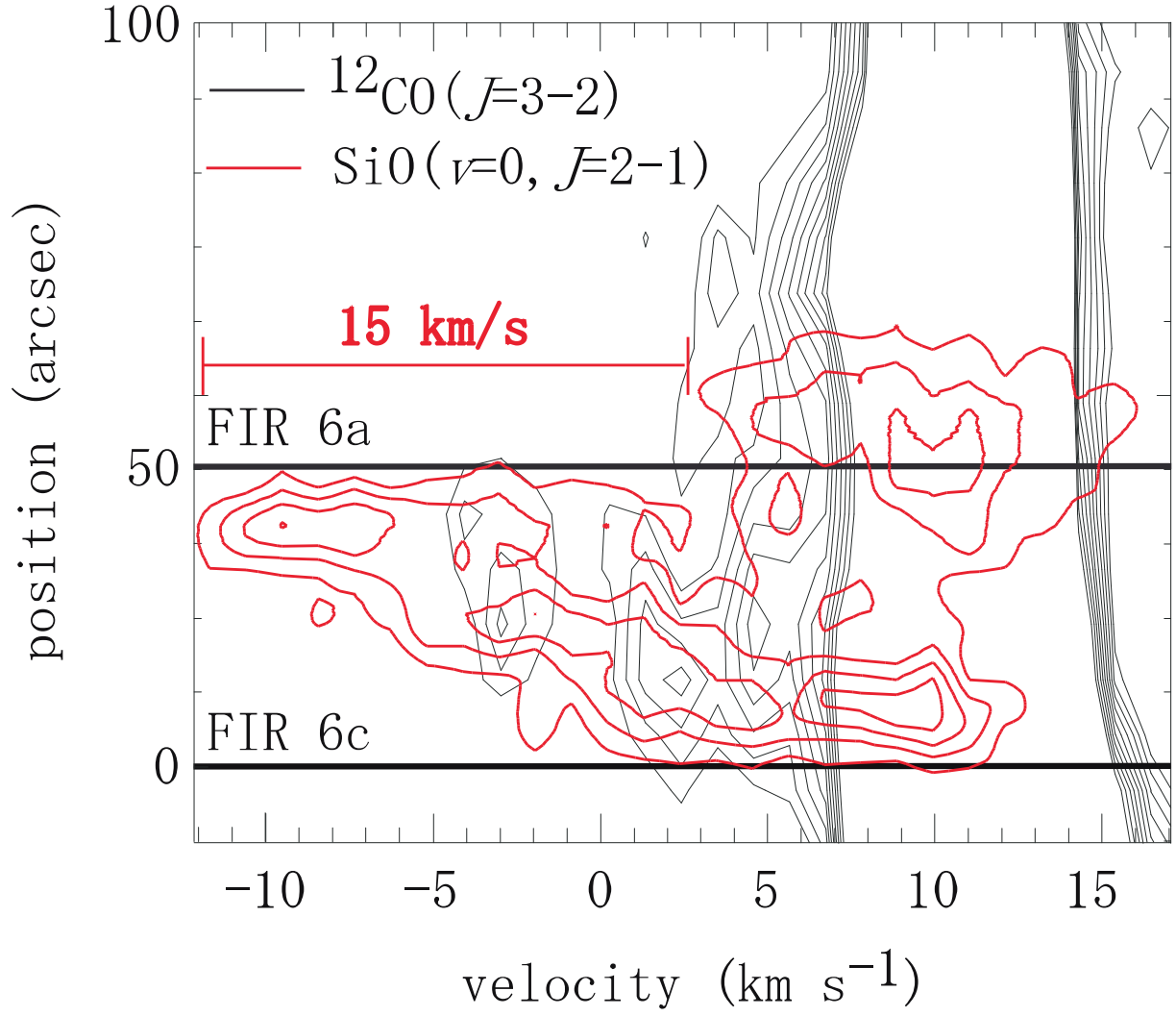


Fig. 6. Position-Velocity diagram of the $^{12}\text{CO} (J=3-2)$; black contour) and the SiO emission (red contour) cut along the axis of the molecular outflow driven by FIR 6c (P.A. = 20°). The vertical axis shows the positional offset with respect to the position of FIR 6c. Horizontal lines show the position of FIR 6a clump and FIR 6c, respectively. Contour levels start at $\pm 5 \sigma$ with an interval of 2.5σ . The rms noise level (1σ) of the SiO and ^{12}CO emission is $0.062 \text{ Jy beam}^{-1}$ and 0.46 K , respectively.

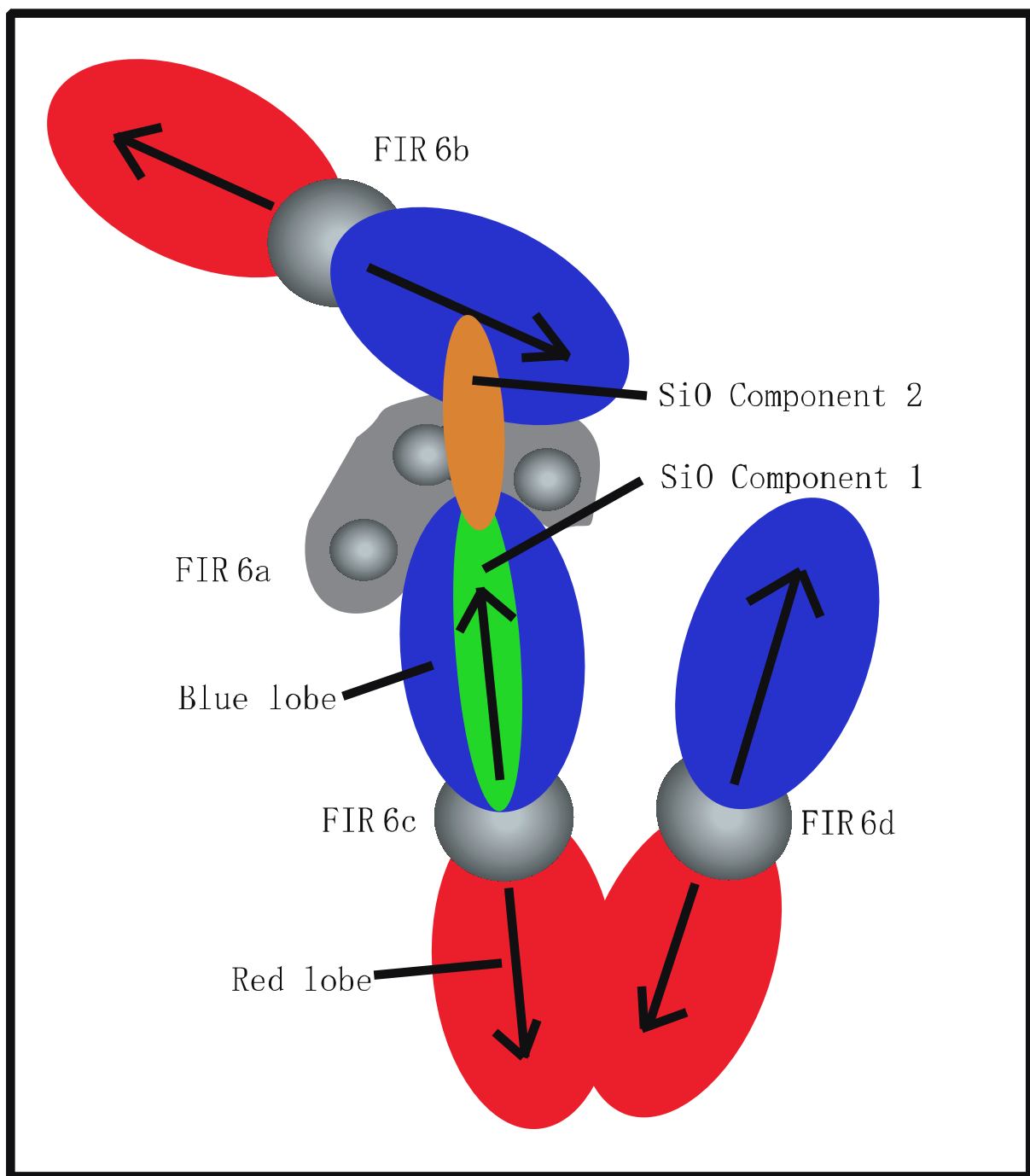


Fig. 7. Schematic picture in the FIR 6 region.

Table 1. PARAMETERS FOR THE MOLECULAR LINE OBSERVATIONS

| Parameter | $^{12}\text{CO } (J=1-0)$ | SiO ($v=0, J=2-1$) |
|--|----------------------------|----------------------------|
| Configuration* | D | |
| Baseline [$k\lambda$] | 3.9-31.4 | 3.3-27.0 |
| Primary beam HPBW [arcsec] | 62 '' | 77 '' |
| Synthesized Beam HPBW [arcsec] | 6.''4 \times 5.''4 | 8.''8 \times 7.''1 |
| Velocity resolution [km s^{-1}] | 0.406 km s^{-1} | 0.539 km s^{-1} |
| Gain calibrator [†] | 0528+134 | |
| Bandpass calibrator [‡] | 3C279 | |
| System temperature in DSB [K] | 200-300 K | 100-300 K |
| Rms noise level [Jy beam^{-1}] | 0.18 Jy beam^{-1} | 0.07 Jy beam^{-1} |

* D is the most compact configuration.

[†] A gain calibrator, 0528+134, was observed every 20 minutes.

[‡] The response across the observed passband was determined from 40 minutes observations.

Table 2. PARAMETERS FOR THE CONTINUUM OBSERVATIONS

| Parameter | Figure 1a | Figure 1b |
|---|---|---|
| Configuration | C & D | |
| Baseline [$k\lambda$] | 2.5-53.1 | |
| Weighting | Natural | Uniform |
| Beam size (HPBW) [arcsec] | 6.''6 \times 4.''9 | 5.''1 \times 3.''8 |
| P.A. of the beam [$^\circ$] | -15.7 | -24.0 |
| Gain calibrator * | 0528+134 | |
| Bandpass calibrator [†] | 3C84, 3C454.3 | |
| System temperature in DSB [K] | 100-300 K | |
| Rms noise level [Jy beam^{-1}] | $9.7 \times 10^{-4} \text{ Jy beam}^{-1}$ | $1.2 \times 10^{-3} \text{ Jy beam}^{-1}$ |

* A gain calibrator, 0528+134, was observed every 20 minutes.

[†] The response across the observed passband was determined from 40 minutes observations.

Table 3. IDENTIFIED DUSTY CORES

| source | α_{J2000} | δ_{J2000} | $D_{maj} \times D_{min}^*$ ($\times 10^3$ AU) | P.A. (degree) | M_{dust}^\dagger M_\odot | n (cm^{-3}) |
|--------|--|------------------|---|------------------|---------------------------------|---------------------------|
| CORE 1 | 05 ^h 35 ^m 55 ^s .6 | -05° 12' 3''.2 | 3.3×2.9 | 178.7 | 1.9 - 5.5 | $1.7 - 4.7 \times 10^7$ |
| CORE 2 | 05 35 22.7 | -05 12 25.2 | 3.9×1.8 | 1.0 | 0.56 - 1.6 | $0.81 - 2.3 \times 10^7$ |
| CORE 3 | 05 35 22.3 | -05 12 27.1 | 1.6×1.1 | 170.5 | 0.18 - 0.51 | $2.1 - 5.8 \times 10^7$ |
| CORE 4 | 05 35 23.0 | -05 12 30.7 | 5.7×2.8 | 157.6 | 0.52 - 1.5 | $0.20 - 0.59 \times 10^7$ |
| CORE 5 | 05 35 21.4 | -05 13 17.0 | 4.8×3.5 | 41.7 | 1.6 - 4.5 | $0.58 - 1.6 \times 10^7$ |
| CORE 6 | 05 35 20.1 | -05 13 15.0 | 2.7×1.8 | 159.4 | 1.4 - 4.0 | $3.5 - 9.9 \times 10^7$ |

* The FWHM size is estimated by the 2-dimensional Gaussian fitting to the uniformly-weighted image.

† Derived from the total flux density integrated within the 3σ contour levels. See texts for details.